Hydrothermally altered mineral mapping using synthetic application of Sentinel-2A MSI, ASTER and Hyperion data in the Duolong area, Tibetan Plateau, China

Bin Hu[a,b], Yongyang Xu[a,b], Bo Wan[a,b,*], Xincai Wu[a,b], Guihua Yi[c]

[a] Department of Information Engineering, China University of Geosciences, Wuhan 430074, China
[b] National Engineering Research Center of Geographic Information System, Wuhan 430074, China
[c] College of Earth Science, Chengdu University of Technology, Chengdu 610059, China

ARTICLE INFO

ABSTRACT

The Duolong area is in a strong potential copper mineralization zone associated with felsic intrusions, and several porphyry copper deposits (PCDs) have been identified. The PCDs are characterized by hydrothermal alteration zones. In this study, Sentinel-2A MultiSpectral Instrument (MSI), Advanced Spaceborne Thermal Emission and Reflection Radiometer (ASTER), and Hyperion data are combined to map hydrothermally altered minerals. Three temporal Sentinel-2A MSI images are processed by integrating the Crosta technique and the anomaly-overlaying selection method to map iron oxides and hydroxyl-bearing minerals. These approaches are implemented to omit interference-induced false anomalies. The six shortwave infrared (SWIR) bands of ASTER are used to extract information on Al-OH and Mg-OH group minerals. The distribution of Al-OH minerals in the ASTER image map corresponds to that of hydroxyl-bearing minerals in the MSI image map. A combination of minimum noise fraction (MNF), pixel purity index (PPI), n-dimensional visualizer (n-D Visualizer) and matched filtering (MF) is adopted to process the Hyperion image to obtain accurate hydrothermal alteration mapping results. The overall accuracy for mineral mapping is 92.75% and the kappa coefficient is 0.89. The results of the Hyperion image are spatially consistent with those of the Sentinel-2A MSI and ASTER images. The image processing results were validated by field investigations and spectral reflectance measurements. Hydrothermally altered rocks correspond well with the five PCDs in the Duolong area. Three mineralization prospects associated with felsic intrusions are discovered in accordance with the results. The methodologies and data are effective in detecting porphyry copper mineralization in other arid areas.

1. Introduction

Porphyry copper deposits (PCDs) supply three-quarters of the world's Cu and one-half of the world's Mo (Sillitoe, 2010). PCDs are characterized by hydrothermal alteration and mineralization zones. Hydrothermally altered minerals have diagnostic spectral absorption properties in the visible and near-infrared (VNIR) through shortwave infrared (SWIR) regions (Pour and Hashim, 2011, 2013).

Remote sensing has been used for hydrothermally altered minerals mapping and mineral prospecting. The Landsat Thematic Mapper (TM), Enhanced Thematic Mapper plus (ETM +), Operational Land Imager (OLI) and Advanced Spaceborne Thermal Emission and Reflection Radiometer (ASTER) data are the four most widely used multispectral data for mapping iron oxides, carbonates and hydroxyl-bearing minerals (Sabins, 1999; Tangestani and Moore, 2000; Goward et al., 2001;

Gabr et al., 2010; Mars and Rowan, 2010; Pour and Hashim, 2012a,b). Compared to the SWIR bands of Landsat data, ASTER SWIR bands provide superior performance in mapping two specific groups of minerals: Al-OHs and Mg-OHs (muscovite, kaolinite, chlorite, epidote and others) (Liu et al., 2017). The methods of spectral feature fitting (SFF), mixture tuned matched filtering (MTMF), matched filtering (MF), spectral angel mapper (SAM), and spectral information divergence (SID) are widely used for hydrothermally altered mineral mapping (Ducart et al., 2006; Zhang and Pazner, 2007; Tangestani et al., 2011; Amer et al., 2012). Supervised machine learning algorithms such as artificial neural network (ANN), decision tree (DT), random forest (RF), support vector machine (SVM), and extreme learning machine (ELM) have been widely used in the image classification (Mas and Flores, 2008; Duro et al., 2012; Chen et al., 2014; Khatami et al., 2016). However, there are few studies on the application of machine learning

---

algorithms for mineral mapping. In the study, hydrothermally altered mineral are mapped using the ELM for the first time.

The European Commission (EC) and European Space Agency (ESA) establish Copernicus, which is the new name for the Global Monitoring for Environment and Security Programme. The Copernicus programme consists of six missions: Sentinel 1–6 (Berger et al., 2012). Sentinel-2A carried a high-resolution multispectral imager with 13 bands spanning the VNIR through SWIR regions. Sentinel-2A MSI (MultiSpectral Instrument) data were first used for geological applications by Van der Meer et al. in 2014, who compared the performance of the Sentinel-2A MSI imager to that of the ASTER imager in mapping hydrothermal areas (Van der Meer et al., 2014). There are a few studies on the use of Sentinel-2A MSI for geological remote sensing (Mielke et al., 2014; Van Der Werff and Van Der Meer, 2016). Principal component analysis (PCA) is usually adopted to process a single-date Landsat TM dataset for the identification of alteration information. Sentinel-2A MSI images processing has been based on band-ratio method so far, however, spatial and spectral performance characteristics of the Sentinel-2A MSI are similar to those of Landsat TM. So, the PCA method can also be used to process a single-date Sentinel-2A MSI dataset. However, field inspections revealed that false anomalies (iron oxides and hydroxyl-bearing minerals) induced by vegetation, cloud, shadow and other factors seriously affected the results. The relevant false anomalies can be effortlessly removed by overlaying selection using multi-temporal Sentinel-2A MSI images.

Hyperspectral remote sensing images can be used to map altered zones and basic surface mineralogy (Kruse et al., 2003; Bedini, 2009; Liu et al., 2016). Hyperion, the first spaceborne imaging spectrometer, is one of three instruments on the Earth Observing-1 (EO-1) spacecraft. However, the application of Hyperion data is limited by its narrow swath and site specificity. The integration of multispectral and hyperspectral data can enable the identification of the type of minerals and increase the reliability of remote sensing-based mineral resources exploration.

The Duolong area in the northern Tibet has a mean elevation of approximately 4900 m. Because of the extremely arid climate, vegetation is sparse in the study area, and altered minerals are exceptionally well exposed. The environment is very harsh because of the rugged topography and severe climate. Elementary alteration zones were delimited by field reconnaissance. The objectives of this study are: (1) to develop a systematic method for identifying hydrothermally altered rocks using Sentinel-2A MSI, ASTER and Hyperion data; (2) to detect crucial minerals associated with felsic intrusions-related mineralization in the Duolong area using Hyperion data; and (3) to discover potentially copper mineralized areas in the Duolong area.

2. Geological setting

The Duolong PCD is one of the largest Cu-Au deposits in Tibet, China (Fig. 1a). The Duolong PCD is in the southern part of the Qiangtang terrane on the western side of the Bangong Co-Nujiang suture zone (BNS, Fig. 1b) (Xu et al., 2017). The Duolong area comprises five PCDs: Duobuza, Bolong, Tiegelong, Naruo, and Saijiao (Fig. 2). The Bangong Co-Nujiang suture zone (BNSZ) extends over 2000 km from Bangong Co to the Nujiang River and is an important porphyry copper metallogenic belt in Tibet.

In the Duolong area, the stratigraphy of the region includes the Lower Jurassic Quse Group, the Middle-Lower Jurassic Sewa Group, the Lower Cretaceous Meiriqie Group, the Paleogene Kangtuo Group and Quaternary deposits (Fig. 2) (Li et al., 2011, 2013). The oldest stratigraphy of the study area, the Quse Group (Lower Jurassic), is mainly distributed in the southern part of the area and consists of metasandstone, siltstone and limestone. The Sewa Group (Middle-Lower Jurassic) contains metasandstone and siltstone, which are widespread in the northeastern part of the study area. Regional intrusive rocks were mainly formed during the Early Cretaceous, and the mineralized rocks

are felsic intrusions (porphyritic granites, porphyritic granodiorites, granodiorites). Tectonism is dominated by nearly NE-EW- and SEE-trending faults. The Duobuza PCD is a deposit which is surrounded by phyllic, argillic and propylitic zones (Zhang et al., 2014). The Bolong PCD is a deposit with an intensive phyllic zone, argillic zone and an undeveloped propylitic zone (Zhu et al., 2011; Yang et al., 2015).

3. Materials

3.1. Sentinel-2A MSI data

Sentinel-2A MSI L1C orthoimage images are downloaded from the Copernicus Open Access Hub. The MSI L1C product is produced from the MSI L1B product by radiometric and geometric corrections. The Sentinel-2 mission is designed to map changes in land cover and to provide data continuity of SPOT, Landsat and ASTER missions. MSI, which is aboard the Sentinel-2A satellite, records solar radiation in 13 bands (Table 1). Cloud-free level L1C (L1C) MSI data acquired on 15th November 2016, 5th December 2016, and 15th December 2016 are used for this research.

3.2. ASTER data

ASTER_07XT is a level 2 product that contains atmospherically corrected data for both the VNIR and SWIR sensors. They are generated using the bands of the corresponding ASTER L1B image. The ASTER L1T data are also generated using the bands of the corresponding ASTER L1B image. The differences between the ASTER_07XT data and the ASTER L1T data are slight (Fig. 3). Because the ASTER L1T product is produced from the ASTER L1B product by precision terrain correction, it is chosen for the study. ASTER L1T radiance data are downloaded from the Land Processes Distributed Active Archive Center (LP DAAC). ASTER measures reflected radiation in three bands between 0.52 and 0.86 μm (VNIR) and in six bands between 1.60 and 2.43 μm (SWIR) with 15-m and 30-m resolution, respectively (Table 1) (Yamaguchi et al., 1999; Rowan et al., 2005). Cloud-free level L1T (L1T) ASTER data acquired on 15th November 2007 are used for this research.

3.3. Hyperion data

Hyperion is a satellite hyperspectral sensor which records data in 242 spectral bands at 30-m spatial resolution, with 7.5 km coverage in the across-track direction (Table 1) (Hubbard et al., 2003). Cloud-free level L1T (L1T) Hyperion data acquired on 30 October 2004 are used for this research. The image is obtained from the USGS Earth Resources Observation and Science (EROS) data center and processed to map iron oxides and hydroxyl-bearing minerals.

3.4. Reflectance spectra

PCDs are characterized by potassic, phyllic, argillic and propylitic zones (Lowell and Guilbert, 1970). In addition, both wall and intrusive rocks can be hydrothermally altered. The alteration zones contain minerals which exhibit diagnostic spectral absorption properties in the VNIR and SWIR wavelength regions (Pour and Hashim, 2012a,b). The broad phyllic alteration zone contains muscovite (sericite), which has an intense Al-OH absorption feature near 2200 nm and a secondary absorption feature near 2350 nm (Fig. 4a) (Hunt, 1977). The narrower argillic alteration zone contains kaolinite, which exhibits intense 2200 nm absorption and a secondary feature at 2170 nm (Fig. 4b) (Hunt, 1977). Epidote and chlorite are common minerals of the outer propylitic zone. Epidote has an intense Mg-OH absorption feature near 2335 nm and a secondary absorption feature near 2250 nm (Fig. 4c) (Hunt, 1977). Limonite has a strong absorption feature at 480 nm and a shallow absorption feature at 930 nm (Fig. 4d) (Hunt, 1977). However,
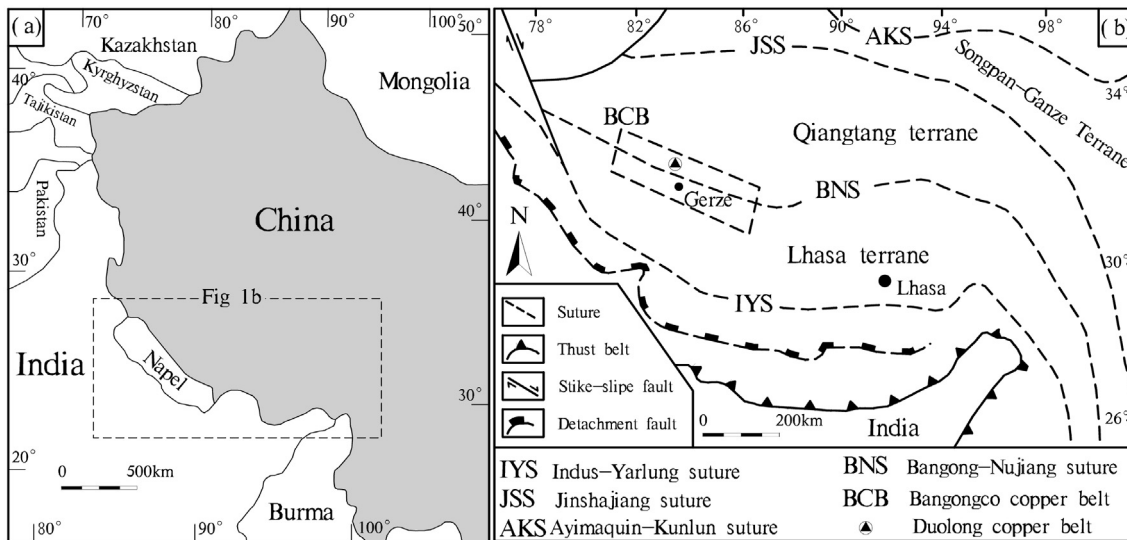
Fig. 1. (a) Geographic map; (b) Sketch geotectonic map and generalized geologic map.

the kaolinite is mostly related to the weathering of feldspars and epidote can be related to regional metamorphism. Kaolinite and epidote anomalies can have a genesis related to deposit when they have a close relationship with muscovite anomalies.

4. Methods and results

4.1. Preprocessing of remote sensing data

The data analyzed in the area are three Sentinel-2A MSI L1C images, a Terra ASTER L1T image and an EO-1 Hyperion L1T image.

The Fast Line-of-sight Atmospheric Analysis of Spectral Hypercubes (FLAASH) is applied to top-of-atmosphere (TOA) level 1C orthoimage products (12 bits signal quantization levels) to retrieve surface reflectance products at a 20-m spatial sampling interval (Table 2) (Berk et al., 1998). The Sentinel-2A MSI L1C images are atmospherically corrected in IDL ENVI version 5.4.1 (Environment for Visualizing Images). Band 10 is removed from the dataset because this band is designed for the detection of cirrus (Drusch et al., 2012). The Sentinel-2A MSI images are subset to the study area (leaving 1195 × 725 pixels starting at the top-left position at x = 973 and y = 2853).

The Terra ASTER L1T dataset (8 bits signal quantization levels, solar

azimuth 166°, solar elevation 37°) is calibrated to radiance data in IDL ENVI version 5.4.1 by applying the gain and offset values. The ASTER image is converted to surface reflectance using the FLAASH (Table 2). To reduce noise in the ASTER SWIR data, minimum noise transform (MNF) analysis is used (Green et al., 1988). The sixth MNF channel contains mostly noise because the eigenvalue of the channel is the minimum. The ASTER SWIR data are compiled by using the inverse MNF the 5 MNF channels. The ASTER SWIR data are subset to the study area (leaving 797 × 484 pixels of 30 × 30 m).

The Hyperion data are processed using a series of methods. First, the EO-1 Hyperion L1T dataset is subset to 132 spectral channels (including bands 11–53, 81–117, 139–164 and 195–220) to exclude unused, overlapping and water absorption bands. Second, Digital Numbers (DNs) are converted to radiance data by applying the gain and offset values. The FLAASH algorithm is adopted to atmospherically correct the Hyperion data with the aerosol amount retrieved by selected dark land pixels (Table 2) (Berk et al., 1998). Third, MNF analysis is adopted to reduce noise in the Hyperion data. The eigenvalues of the last three MNF channels (channels 130, 131, 132) are 1.72, 1.70, and 1.69, respectively. The Hyperion data are compiled using inverse MNF channels 1 through 129 to remove the noise in the Hyperion data.

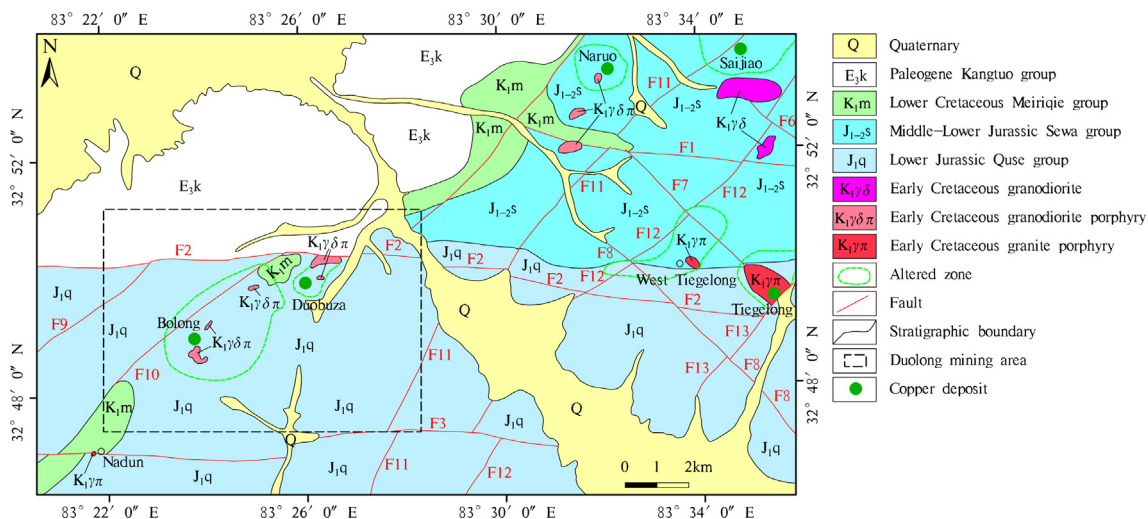The image process in this study follows the sequence of steps

Fig. 2. Geological map of the study area.

Table 1
Performance parameters for the Sentinel-2A MSI, ASTER and Hyperion sensors.

Sensors	Subsystem	Band Number	Spectral Range (µm)	Spatial Resolution	Ltypical SNR[1]	Signal Quantization Levels
MSI	VNIR	1	0.433–0.453	60 m	129	12 bits
		2	0.458–0.523	10 m	154	12 bits
		3	0.543–0.578	10 m	168	12 bits
		4	0.650–0.680	10 m	142	12 bits
		5	0.698–0.713	20 m	117	12 bits
		6	0.733–0.748	20 m	89	12 bits
		7	0.773–0.793	20 m	105	12 bits
		8	0.785–0.900	10 m	172	12 bits
		8a	0.855–0.875	20 m	72	12 bits
		9	0.935–0.955	60 m	114	12 bits
	SWIR	10	1.360–1.390	60 m	50	12 bits
		11	1.565–1.655	20 m	100	12 bits
		12	2.100–2.280	20 m	100	12 bits
ASTER	VNIR	1	0.52–0.60	15 m	370	8 bits
		2	0.63–0.69	15 m	306	8 bits
		3N	0.78–0.86	15 m	202	8 bits
		3B	0.78–0.86	15 m	183	8 bits
	SWIR	4	1.600–1.700	30 m	466	8 bits
		5	2.145–2.185	30 m	254	8 bits
		6	2.185–2.225	30 m	229	8 bits
		7	2.235–2.285	30 m	234	8 bits
		8	2.295–2.365	30 m	258	8 bits
		9	2.360–2.430	30 m	231	8 bits
Hyperion	VNIR	Continuous	0.400–1.000	30 m	161	16 bits
	SWIR	Continuous	1.000–2.500	30 m	40	16 bits

[1] SNR at specified levels of typical spectral radiance (Typical).

summarized in the flowchart of Fig. 5.

4.2. Sentinel-2A MSI data analysis

Hydroxyl-bearing minerals, which have a spectral diagnostic feature in the 2.10–2.28 µm, can cause low reflectance in the Sentinel-2A MSI band 12. These minerals also have a very high reflectance in the Sentinel-2A MSI band 11. In addition, Sentinel-2A MSI band 1–9 (VNIR) can discriminate iron oxides (limonite and goethite), which cause low reflectance in the Sentinel-2A MSI band 2 and high reflectance in band 4. The Crosta technique is a PCA method which adopts the association of Landsat TM bands 1, 4, 5 and 7 to extract hydroxyl-bearing minerals and the association of Landsat TM bands 1, 3, 4 and 5 for iron oxides (Loughlin, 1991). Similarly, hydroxyl-bearing minerals are extracted by the combination of Sentinel-2A MSI bands 2, 8a, 11, 12 and the iron oxides are extracted by the combination of Sentinel-2A MSI bands 2, 4, 8a, 11. However, interference factors such as snow, ice, water and soil can cause false anomalies. Masking technique is employed to eliminate the interference of the aforementioned factors. In addition, false anomalies caused by random noise can be confused with real alteration zones. The altered anomalies are usually contained in the noisiest principal component (commonly the third or fourth principal component) (Singh and Harrison, 1985; Liu et al., 2011, 2013).

The real alteration zones do not change, whereas the false anomalies induced by noise are randomly distributed. The noise-caused false anomalies can be eliminated by overlaying selection using multi-temporal Sentinel-2A MSI images (Langford, 2015; Liu et al., 2017). Conditions of climate, season, weather or atmosphere could be very different for data acquired on different dates. We had better select the images which are photographed in the similar seasons. An anomaly-overlaying selection method is proposed to remove the noise-caused false anomalies because they do not coincide with those of other images. The Crosta technique and anomaly-overlaying selection method are used to extract information on hydroxyl-bearing minerals
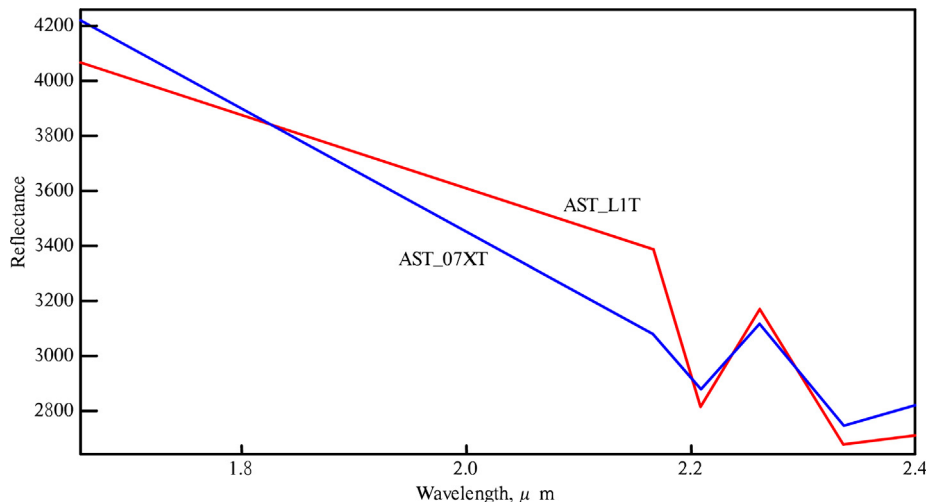

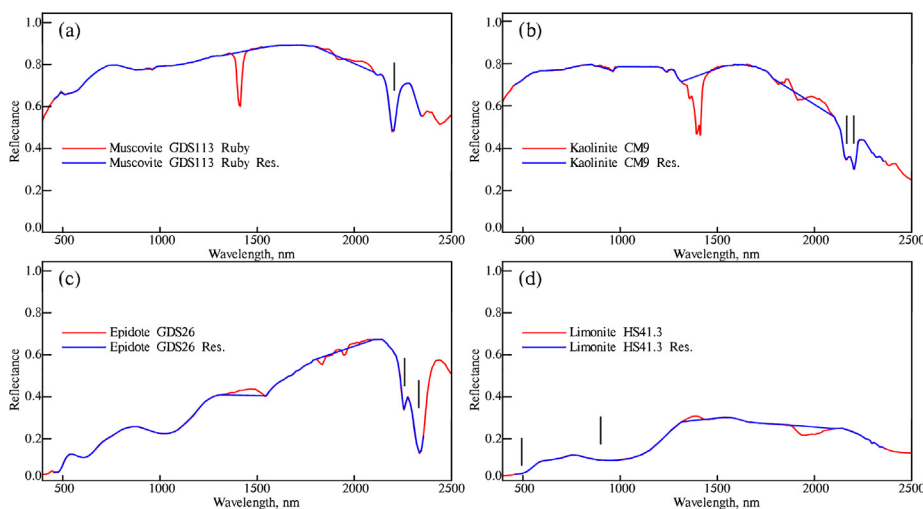**Fig. 3.** The reflectance spectra of AST_07XT and AST_L1T data at the same location.

Fig. 4. Laboratory reflectance spectra of minerals from the USGS spectral library (red line) and spectra resampled to Hyperion 132 bands (blue line). The vertical lines show the location of important absorption features. (For interpretation of the references to color in this figure legend, the reader is referred to the web version of this article.)

Table 2
FLAASH parameters for the Sentinel-2A MSI, ASTER and Hyperion images.

	Atmospheric Model	Aerosol Model	Aerosol Retrieval
Sentinel-2A MSI	Mid-Latitude Summer	Tropospheric	2-Band (K-T)
ASTER	Mid-Latitude Summer	Tropospheric	No
Hyperion	Mid-Latitude Summer	Tropospheric	2-Band (K-T)

and iron oxides.

The band combination of TM 1, 4, 5, 7 is used to extract the information of hydroxyl-bearing minerals (Liu et al., 2017). Similarly, the band combination of Sentinel-2A MSI 2, 8a, 11, 12 can be used to extract the information concerning hydroxyls. The PC3s of the band combination of 2, 8a, 11, 12 using the Crosta technique primarily contain information concerning hydroxyls because of the greatest loading of band 11 (-0.474 to -0.507) and band 12 (0.836–0.841) (Table 3). The hydroxyls occur as dark pixels because the positive loading at band 12 and the bands need to be inversed. Many researches have demonstrated that PC3 and PC4 have nearly normal distributions. The anomalies for hydroxyl-bearing minerals are determined based on a threshold of $\mu + 2\ast\sigma$, where μ and σ represent the mean value and standard deviation of the relevant principal component images, respectively. The three threshold values are 152.64, 155.81 and 149.01 for the images obtained from Sentinel-2A data acquired on 15th November 2016, 5th December 2016, and 15th December 2016, respectively (Fig. 6a, b and c). The anomaly-overlaying selection method is employed to eliminate the noise-induced anomalies. A pixel is classified as a real anomaly if it satisfy the aforesaid criterion (Fig. 6d). The mineral information of iron oxides is extracted using the same process. Finally, the iron oxides and hydroxyl-bearing minerals are overlaid on

Table 3
The Eigenvector matrix values of the PCA for the 2, 8a, 11, 12 bands of all three multi-temporal MSI images.

15th Nov. 2016	Band 2	Band 8a	Band 11	Band 12
PC 1	0.129	0.423	0.715	0.541
PC 2	0.502	0.704	−0.502	−0.006
PC 3	−0.144	−0.228	−0.474	0.838
PC 4	0.843	−0.523	0.108	0.064

5th Dec. 2016	Band 2	Band 8a	Band 11	Band 12
PC 1	0.138	0.436	0.715	0.528
PC 2	0.578	0.666	−0.466	−0.070
PC 3	−0.130	−0.152	−0.503	0.841
PC 4	−0.794	0.585	−0.133	−0.096

15th Dec. 2016	Band 2	Band 8a	Band 11	Band 12
PC 1	0.120	0.417	0.724	0.536
PC 2	0.562	0.690	−0.453	−0.052
PC 3	−0.147	−0.150	−0.507	0.836
PC 4	−0.805	0.572	−0.115	−0.109

the false color composite Sentinel-2A image (MSI bands 12 (red), 8a (green), 2 (blue)).

Fig. 7 shows the final result for the altered minerals derived from multi-temporal Sentinel-2A MSI data. The iron oxides are depicted as red pixels and the hydroxyl-bearing minerals as yellow pixels. Some iron oxides are distributed in the proximity of the Quse Group and Meiriqie Group (A and B, red, Fig. 7), whereas the other anomalies cluster around the granite porphyry in the Tiegelong deposit (C, red, Fig. 7). Nevertheless, most of the iron oxides are disorganized and show no obvious correlation with the felsic intrusions. The hydroxyl-bearing
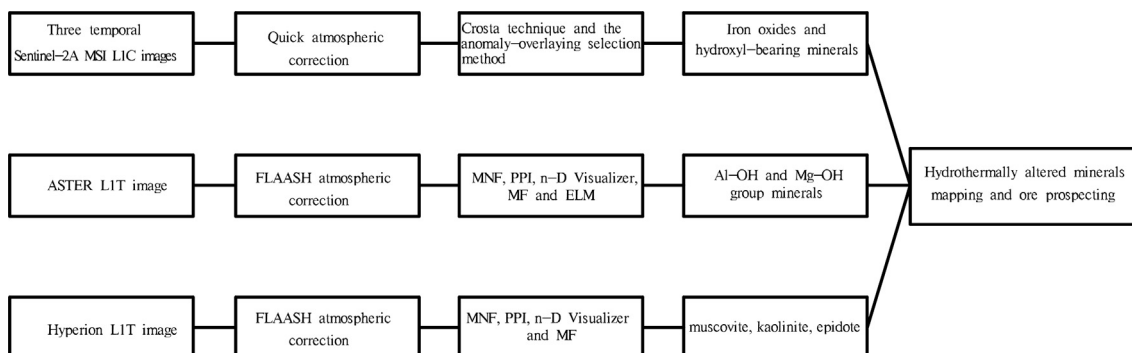

Fig. 5. Sentinel-2A MSI, ASTER and Hyperion data processing flowchart.
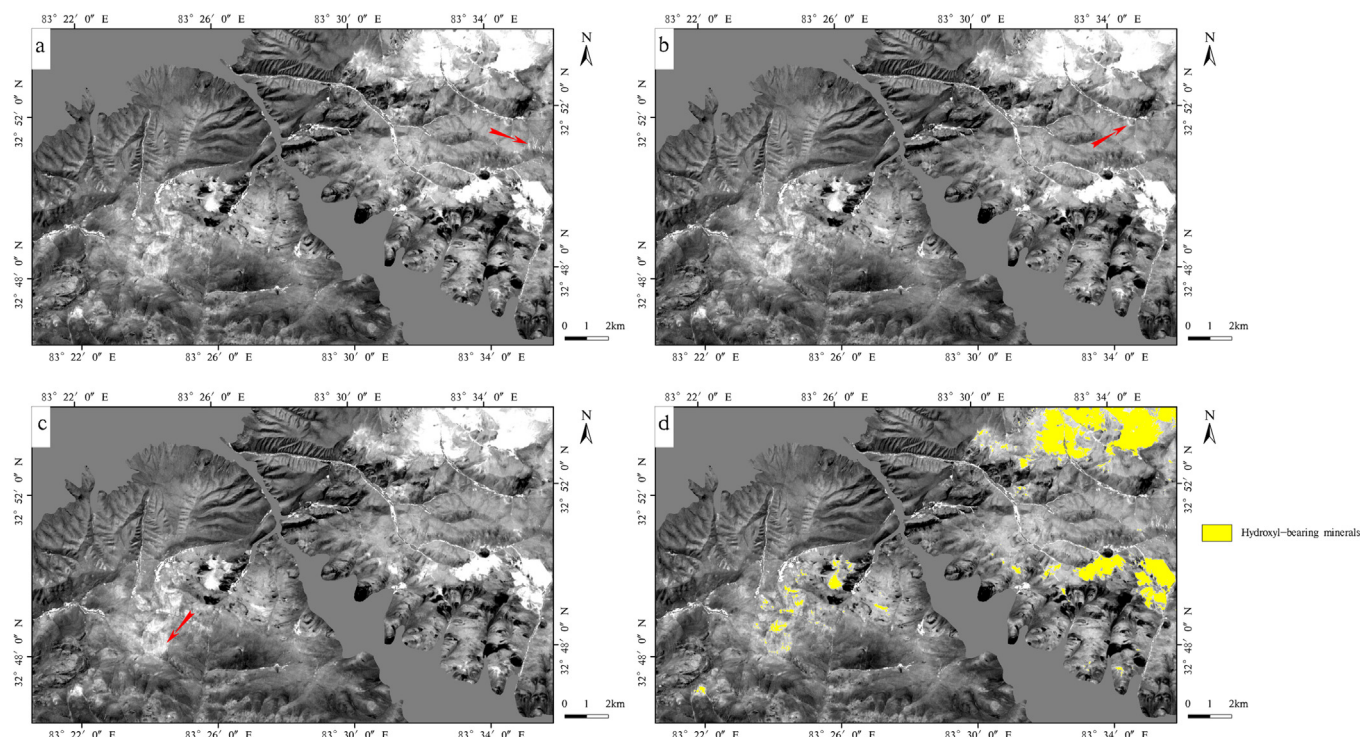
Fig. 6. Results of hydroxyl-bearing minerals extracted by using Crosta technique. (a) Results of 15th November 2016, (b) Results of 5th December 2016, (c) Results of 15th December 2016 and (d) Results of hydroxyl-bearing minerals extracted by using Crosta technique and 3 scenes anomaly-overlaying selection. Red arrows point to the pixels extracted as high value only in one image. (For interpretation of the references to color in this figure legend, the reader is referred to the web version of this article.)
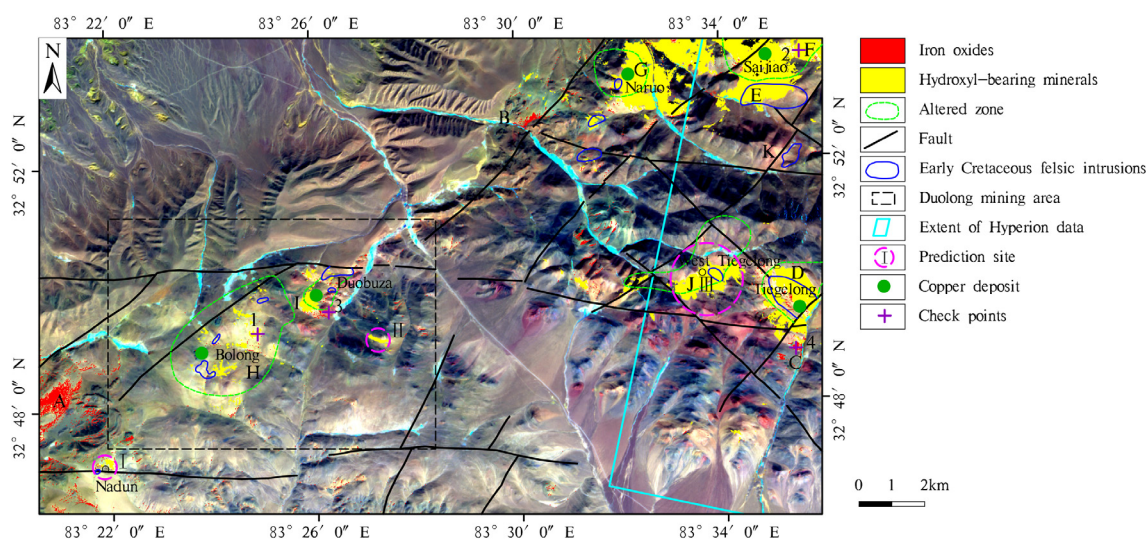

Fig. 7. Results for hydroxyl-bearing minerals and iron oxides extracted using the Crosta technique and three scenes of the anomaly-overlaying selection. Background image: MSI 12, 8a, 2 in RGB (15th November 2016). Areas discussed in the text: (A) iron oxides in the proximity of the Quse Group; (B) iron oxides in the proximity of the Meiriqie Group; (C) iron oxides in hydrothermally altered rocks of the Tiegelong deposit; (D) hydroxyl-bearing minerals in granite porphyry of the Tiegelong deposit; (E) hydroxyl-bearing minerals inside granodioritic intrusive rocks of the Saijiao deposit; (F) hydroxyl-bearing minerals around granodioritic intrusive rocks of the Saijiao deposit;(G)hydroxyl-bearing minerals in granodiorite porphyry of the Naruo deposit; (H) hydroxyl-bearing minerals around granodiorite porphyry of the Bolong deposit; (I) hydroxyl-bearing minerals around granodiorite porphyry of the Duobuza deposit; (J) hydroxyl-bearing minerals in hydrothermally altered rocks of the West Tiegelong area; (K) granodiorite in the northeastern part of the study area.

minerals are distributed near the central and east regions, where the granodiorites, granodiorite porphyries and granite porphyries occur on the map. Hydroxyl-bearing minerals mainly occur in the felsic intrusions (blue color) and agree well with all of the deposits (D, E, F, G, H and I, yellow, Fig. 7). Moreover, the hydroxyl-bearing minerals show an obvious correlation with the preliminary alteration zones delimited by ground exploration. Only one felsic intrusion has anomalies associated

with both iron oxides and hydroxyl-bearing minerals (D, yellow, Fig. 7), whereas hydroxyl-bearing minerals are inside or around the other eleven felsic intrusions (J, yellow, Fig. 7). Iron oxides and hydroxyl-bearing minerals have not been detected in the granodiorite in the northeastern part of the study area (K, Fig. 7).

Table 4
The Eigenvector matrix values of the PCA for the 1, 3, 4, 6 bands of ASTER L1T image.

15th Nov. 2007	Band 2	Band 8a	Band 11	Band 12
PC 1	−0.384	−0.540	−0.635	−0.397
PC 2	−0.693	−0.366	0.547	0.293
PC 3	−0.037	−0.004	−0.511	0.859
PC 4	−0.608	0.758	−0.191	−0.136

4.3. ASTER data analysis

The PCA and band-ratio techniques are usually used to map hydrothermally altered minerals. Band ratios are often derived using laboratory-measured or field-measured spectra, however, band ratios such as those published by Commonwealth Scientific Industrial Research Organization (CSIRO) are more of the standard (Hewson et al., 2015). These band ratios are not defined in a laboratory, but have been defined on ASTER scenes acquired all over Australia. Some of these ratios are specifically for masking vegetation, snow, etc. In general, these band ratios are therefore least affected by vegetation and other covers. The Crosta technique, which involves principal component (PC) transformation of band ratios, uses laboratory spectra to identify the bands to be used for different alteration minerals. The PC3 of the band association of 1, 3, 4 and 6 for the ASTER image primarily hold the information concerning Al-OH group minerals (Table 4) (Moore et al., 2008). It should be inversed to be represented as bright pixels (Fig. 8b). RBD6 [(ASTER band 4 + ASTER band 7)/ASTER band 6] image is used to delineate phyllic mineral assemblages (Fig. 8c) (Mars and Rowan 2006).

Al-OH group minerals include muscovite, illite and kaolinite. Both muscovite and kaolinite show an intense absorption feature near 2200 nm (coinciding with ASTER band 6). Mg-OH group minerals

include epidote and chlorite. Epidote and chlorite have a spectral absorption feature near 2335 nm (coinciding with ASTER band 8). It is difficult to identify epidote and chlorite using an ASTER SWIR image. Whereas, ASTER SWIR bands have sufficient spectral resolution to distinguish Al-OH group minerals from Mg-OH group minerals (Rowan and Mars, 2003). Trials have shown that endmember selection utilizing the entire coverage of the image does not provide satisfactory consequences (Hubbard et al., 2003). The Tiegelong area consists of a vast variety of surficial materials, including volcanic rocks, felsic intrusions, hydrothermally altered rocks, snow, ice and rivers. The methods of minimum noise fraction (MNF), pixel purity index (PPI) and n-dimensional visualizer (n-D Visualizer) are used to extract reflectance spectra from the ASTER image subset in the Tiegelong area. The scatter plot of endmember is shown in Fig. 9. The locations of the purest pixels are illustrated in the following image (Fig. 10).

The endmember spectra acquired from the ASTER image exhibit Al-OH and Mg-OH spectral absorption features (Rowan et al., 2006). The reflectance spectrum of the Al-OH minerals displays strong 2200 nm and weak 2350 nm absorption features (A, yellow, Fig. 11) (Zhang et al., 2016). The Mg-OH minerals have a well-defined absorption feature positioned at 2335 nm (B, magenta, Fig. 11) (Zhang et al., 2016). The MF procedure is applied to analyse the ASTER SWIR bands using the ASTER image reference spectra. The MF is a partial unmixing technique which maximizes the response of the known endmember and suppresses the background (Rowan et al., 2004). It is expressed as:

$$\text{MF}(\mathbf{x}) = (\mathbf{t}-\mathbf{m})^{\text{T}}\mathbf{S}^{-1}(\mathbf{x}-\mathbf{m}) \tag{1}$$

where **t** is the target vector, **x** is the sample vector, **m** is the background mean and **S** is the background covariance. The resulting MF (**x**) is the threshold to control the false alarm rate (Bedini, 2011). The MF result is normally distributed and pixels with a greater value contain higher contents of the target component (Liu et al., 2017). The MF image (Fig. 8d) is found to be sharper and easier to interpret than the images produced by the PCA and band-ratio methods (Fig. 8b and c). Pixels
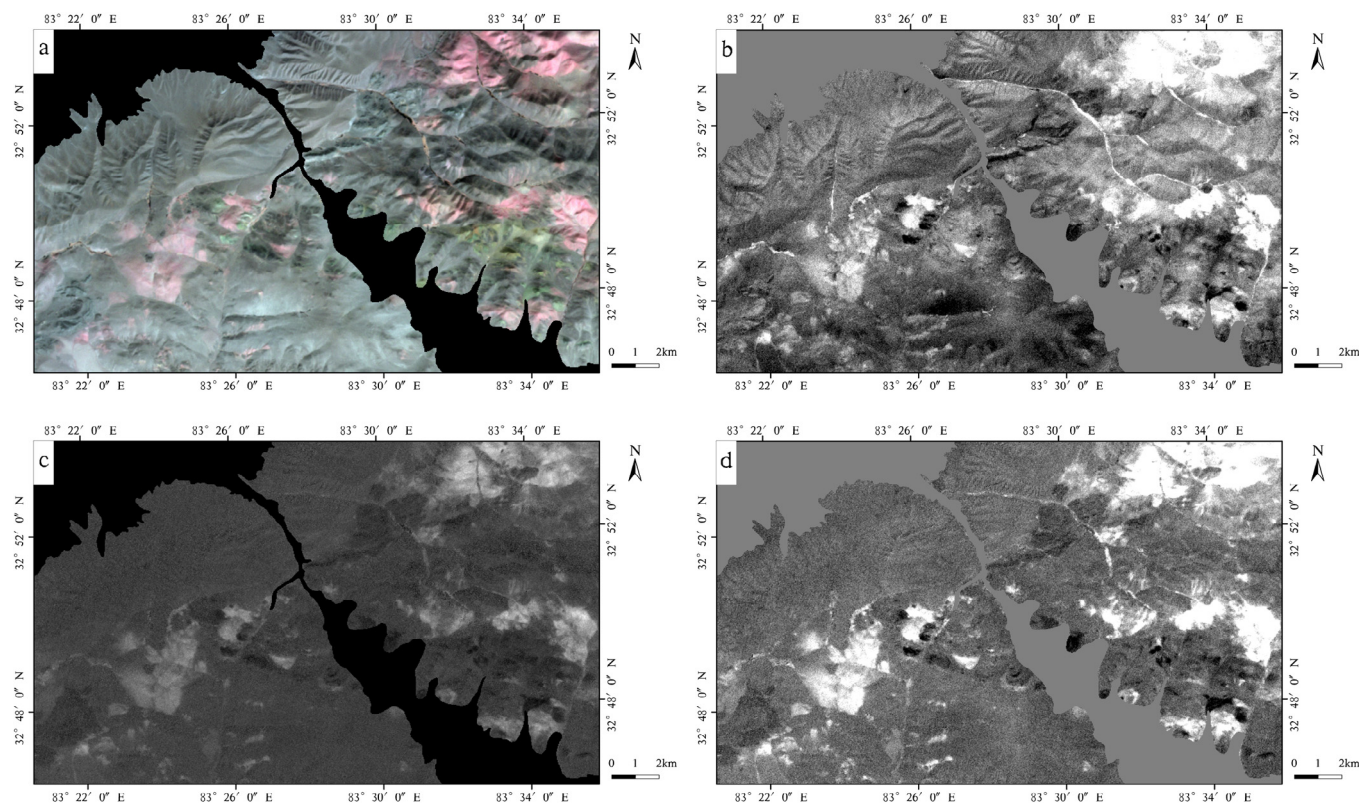

Fig. 8. (a) False color composite image using ASTER 4, 6 and 8. (b) Results of Al-OH group minerals extracted by using Crosta technique. (c) Results of RBD6 band and (d) Results of MF analysis for Al-OH group minerals.
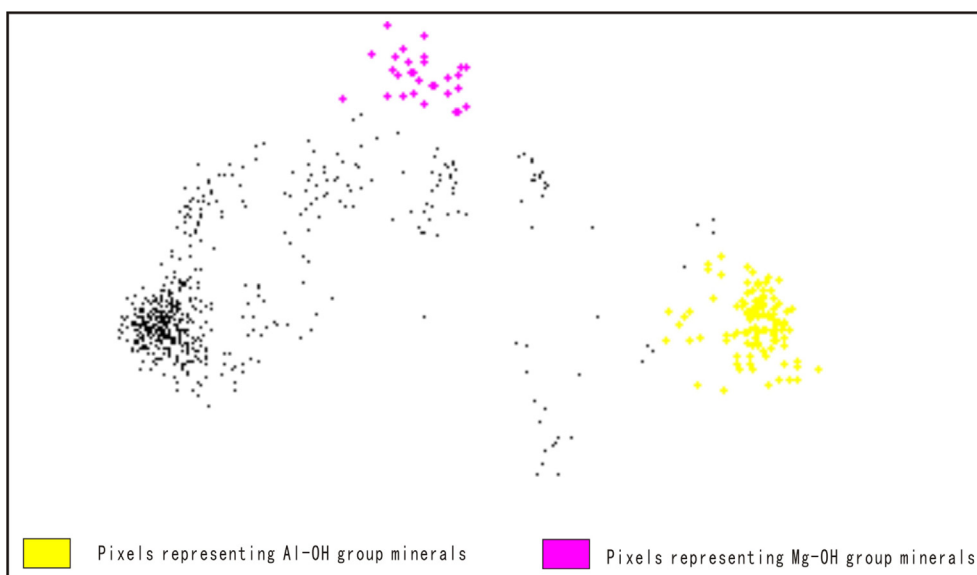
Fig. 9. The scatter plot of endmember extracted by a combination of MNF, PPI and n-D Visualizer.
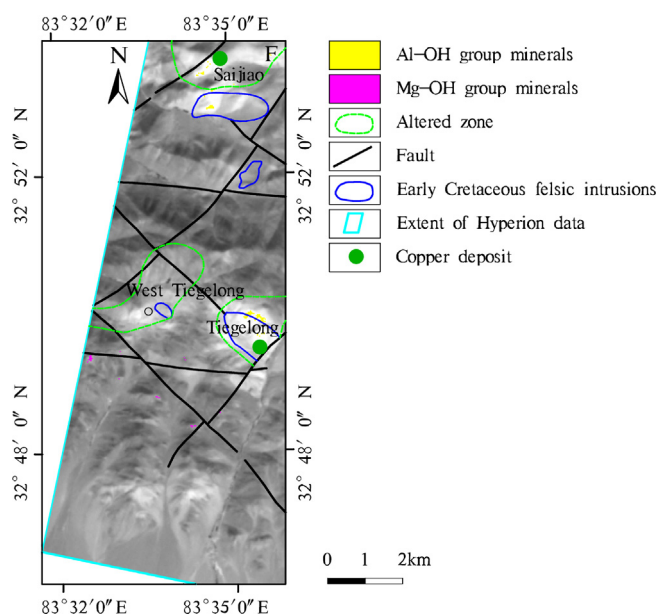

Fig. 10. The location of the purest pixels in the Tiegelong area. Background image is ASTER band 4.

Fig. 11. Reflectance spectra of hydrothermally altered minerals from the ASTER image subset. ASTER band centers shown at the top.

representing Al-OH group minerals are extracted from the ASTER SWIR image in the Tiegelong area. Approximately 30 percent of the pixels are randomly selected to show the distribution of Al-OH group minerals, reserving the others as a "hold-out" test set. The test set is used to quantitatively evaluate the image processing results. The area under the receiver operating characteristic (ROC) curve (AUC) is used as a performance measure. The three values of AUC are 0.9984, 0.9983, 0.9993, respectively. The results indicate that the MF method outperform the PCA and band-ratio methods. It is implemented in Matlab 2017a software. Each anomaly is determined by a threshold value $\mu + 2*\sigma$, where μ and σ represent the mean value and standard deviation of the relevant band, respectively. Hence, the threshold values of the Al-OH and Mg-OH minerals are set as 0.34 and 0.32, respectively.

The hydrothermally altered minerals are mapped in the study area using the ASTER SWIR image reference spectra (Fig. 12). The yellow areas representing Al-OH minerals correspond well with the distribution of hydroxyl-bearing minerals in the MSI image map (yellow,
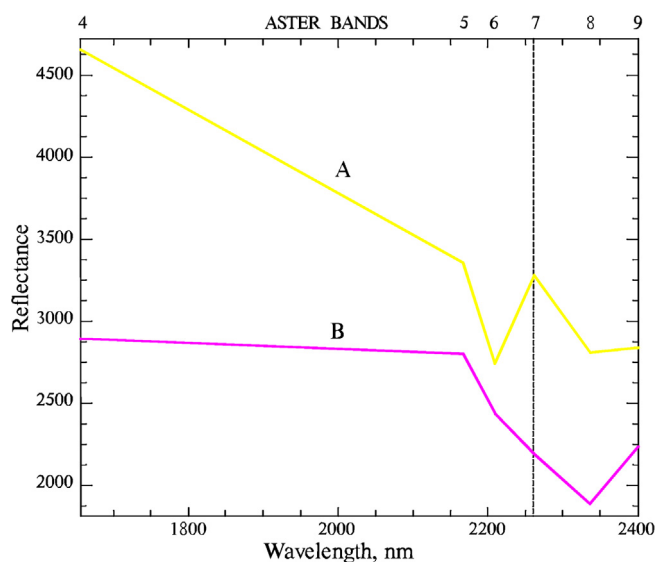
Figs. 12 and 7). The Al-OH group minerals are mainly distributed in the central and eastern parts of the study area. The results show the dominance of Al-OH minerals in the granitic intrusive rocks in the eastern part of the area (D, yellow, Fig. 12), inside and around the granodiorite in the northeasternmost part of the area (E and F, yellow, Fig. 12), in the northeastern labelled granodiorite porphyry (G, yellow, Fig. 12), in the granodiorite porphyry of the Bolong deposit (H, yellow, Fig. 12) and in the granodiorite porphyry of the Duobuza deposit (I, yellow, Fig. 12). The Al-OH minerals mainly occur in the proximity of felsic intrusions (blue color) and correspond very well with the five deposits (D, E, F, G, H and I, yellow, Fig. 12). Moreover, Al-OH minerals cluster inside and around granite porphyry in the West Tiegelong area situated in the eastern part (J, yellow, Fig. 12). The information on Mg-OH minerals is illustrated as magenta pixels (magenta, Fig. 12). A few Mg-OH minerals are scattered around the granodiorite in the northeastern part (K, magenta, Fig. 12), whereas no anomaly has been identified from the MSI image (K, Fig. 7). Mg-OH minerals are mostly distributed to the south of the two granite porphyries in the southeastern part (L, magenta, Fig. 12). Some Mg-OH minerals are mapped around the granodiorite
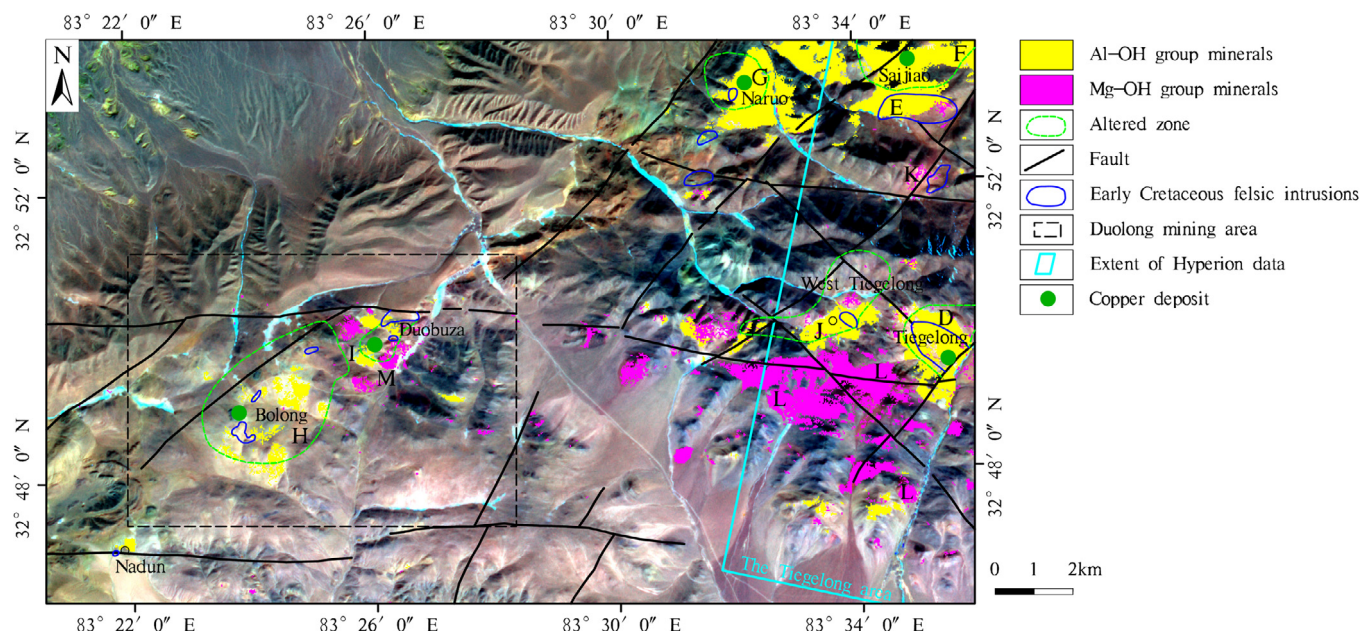
Fig. 12. Results for Al-OH group minerals and Mg-OH group minerals extracted using the MF procedure. Background image: ASTER 6, 3, 1 in RGB (15th November 2007). Areas discussed in the text: (D) Al-OH minerals in the granitic intrusive rocks of the Tiegelong deposit; (E) Al-OH minerals in the granodiorite in the northeastern part; (F) Al-OH minerals around the granodiorite in the northeastern part; (G) Al-OH minerals in the northeastern labelled granodiorite porphyry; (H) Al-OH minerals in the granodiorite porphyry of the Bolong deposit; (I) Al-OH minerals in the granodiorite porphyry of the Duobuza deposit; (J) Al-OH minerals cluster inside and around the granite porphyry in the West Tiegelong area; (K) Mg-OH minerals around the granodiorite in the northeastern part; (L) Mg-OH minerals in the hydrothermally altered rocks in the southeastern part; (M) Mg-OH minerals mapped in the Duobuza deposit.

porphyry of the Duobuza deposit (M, magenta, Fig. 12). In the Bolong PCD, the alteration minerals of the phyllic zone are mainly composed of muscovite and silicide (Zhu et al., 2011; Yang et al., 2015). Nevertheless, the propylitic zone of Bolong PCD is undeveloped (Yang et al., 2015). In the Duobuza PCD, the phyllic zone mainly consists of sericicitization and silicification (Zhang et al., 2014; Zhang et al., 2016). Strong muscovite alteration is apparent in the granodiorite porphyry (Sun et al., 2017).

Machine learning algorithms (MLAs) are automated means which can be used for data-driven classification (Zhou et al., 2018; Cracknell and Reading, 2014). Huang et al. put forward the ELM, which is based on a single hidden layer neural network (Huang et al., 2006). The ELM has been used for remote sensing classification (Pal, 2009). Only one user-defined parameter is need when the ELM classifier is used for remote sensing classification. What is more, the performance of the ELM is usually more excellent than that of the back-propagation neural network. The 14,978 training pixels are extracted by the MNF, PPI and n-D Visualizer. The ELM algorithm is implemented in Matlab 2017a software. The number of hidden nodes in hidden layer is set as 1000. The results of ELM classification method are shown in Fig. 13. The result of ELM algorithm corresponds to that of MF algorithm (yellow and magenta, Figs. 12 and 13).

4.4. Hyperion data analysis

Two spectral subsets of Hyperion bands are processed separately to detect iron oxides and hydroxyl-bearing altered mineral assemblages. The first subset of Hyperion data covering 80 bands (bands 11–53 and 81–117 with wavelengths at 457–884 nm and 952–1316 nm) is used to highlight iron oxide information. The second subset of Hyperion data covering 31 bands (bands 146–150 and 195–220 with wavelengths at 1608–1648 nm and 2102–2355 nm) is analyzed to extract hydroxyl-bearing altered minerals. Reference spectra can be selected from the image or spectral libraries (Liu et al., 2017). Generally, reference spectra acquired from the image are more available for target detection because they are obtained under the same atmospheric conditions as

the image (Bedini, 2011). The PPI procedure is performed on the top 15 MNF bands to map endmember spectra, because the top 15 MNF bands contain most of the spectral information (Kruse et al., 2003). The potential endmember spectra are loaded into an n-dimensional (n-D) scatterplot and rotate until "points" or extremities on the scatterplot are exposed. Once a set of unique pixels is defined using the n-D analysis technique, each separate projection on the scatterplot is exported to a region of interest (ROI) in the image (Kruse et al., 2003). Each class is identified by comparisons of the endmember spectra to USGS spectral libraries (Rowan et al., 2003; Pour et al., 2013; Molan et al., 2014). The Hyperion image spectra selected from the Hyperion SWIR bands are used to map the spatial distribution of the altered minerals (Pour and Hashim, 2011; Kratt et al., 2010). The muscovite spectrum displays an Al-OH absorption feature centered near 2200 nm (A, yellow, Fig. 14). The spectrum, which exhibits a diagnostic doublet Al-OH absorption feature in the 2170–2200 nm region, represents kaolinite (B, green, Fig. 14). Epidote is characterized by an intense Mg-OH absorption feature near 2335 nm and a distinctive feature at 2250 nm (C, magenta, Fig. 14).

The results of the MF analysis of the Hyperion SWIR bands (1608–2355 nm) for muscovite, kaolinite and epidote are shown in Fig. 15. The MF results are normally distributed and the threshold value of each anomaly is determined by the value $\mu + 2*\sigma$. Note: μ and σ represent the mean value and standard deviation of the relevant image, respectively. The threshold values of muscovite, kaolinite and epidote are set as 0.30, 0.22 and 0.27, respectively. Classification aggregation tool is used to solve the problem of isolated pixels occurring in classification image. It is difficult to obtain a large amount of rock samples because of the area's remoteness, severe climate, and rugged topography. Thus, virtual verification is performed to evaluate the image processing results. Pixels representing muscovite, kaolinite and epidote are extracted from the Hyperion SWIR image. Approximately 30 percent of the pixels are randomly selected to extract the reference spectra and the others are selected to assess the accuracy of the results. The total accuracy for hydrothermally altered mineral mapping is 92.75%, and the kappa coefficient is 0.89 (Table 5) (Wan et al., 2015). The
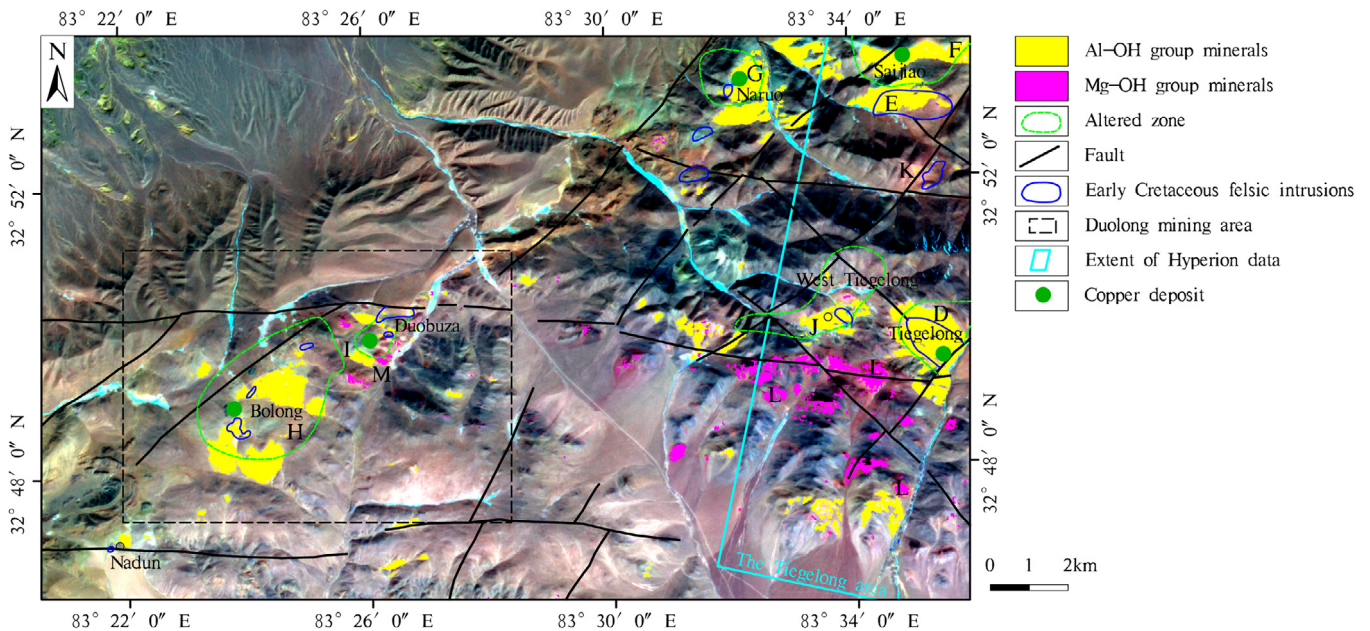
Fig. 13. Results for Al-OH group minerals and Mg-OH group minerals extracted using the ELM algorithm. Background image: ASTER 6, 3, 1 in RGB (15th November 2007). Areas discussed in the text :(D) Al-OH minerals in the granitic intrusive rocks of the Tiegelong deposit; (E) Al-OH minerals in the granodiorite in the northeastern part; (F) Al-OH minerals around the granodiorite in the northeastern part; (G) Al-OH minerals in the northeastern labelled granodiorite porphyry; (H) Al-OH minerals in the granodiorite porphyry of the Bolong deposit; (I) Al-OH minerals in the granodiorite porphyry of the Duobuza deposit; (J) Al-OH minerals cluster inside and around the granite porphyry in the West Tiegelong area; (K) Mg-OH minerals around the granodiorite in the northeastern part; (L) Mg-OH minerals in the hydrothermally altered rocks in the southeastern part; (M) Mg-OH minerals mapped in the Duobuza deposit.

difference between the muscovite spectrum and the kaolinite spectrum is relatively subtle (Figs. 4 and 14). As a result, the accuracy for muscovite detection is 85.71% because a small number of muscovite areas (approximately 14.29%) are misclassified as kaolinite.

Three classes of hydrothermally altered minerals are mapped in the Tiegelong area using the Hyperion image spectra (Fig. 16). The yellow areas representing muscovite correspond to the Al-OH minerals in the ASTER image map (yellow, Figs. 12 and 16). The exposures of muscovite are more scattered than the Al-OH minerals in the ASTER image map. The green pixels, which indicate kaolinite, are concentrated in the proximity of granodiorite (F, green, Fig. 16). However, the Al-OH minerals are mapped at location F in the ASTER image map (F, yellow, Fig. 12). The magenta color in the Hyperion image represents epidote (magenta, Fig. 16). Very few Mg-OH minerals have been detected around the granodiorite in the northeastern part (K, magenta, Fig. 16).

In area L, the epidote is less widespread in the Hyperion image map than the Mg-OH minerals in the ASTER image map (L, magenta, Figs. 12 and 16).

The results suggest that it could be erroneous to distinguish muscovite from kaolinite using the ASTER SWIR image, which is a new conclusion in the field. The transformed divergence (TD) is a common measure ranging from 0 (no separability) to 2 (completely separable) (Huang et al., 2016). It is expressed as:

$$D = \frac{1}{2} tr \left[(C_1 - C_2)(C_1^{-1} - C_2^{-1}) \right] + \frac{1}{2} tr \left[(C_1^{-1} - C_2^{-1})(\mu_1 - \mu_2)(\mu_1 - \mu_2)^T \right]$$

$$TD = 2 \left[1 - \exp\left(-\frac{D}{8} \right) \right]$$

C_1 is the covariance matrix of class 1, μ_1 is the mean vector of class 1, tr is the matrix trace function, and T is the matrix transposition
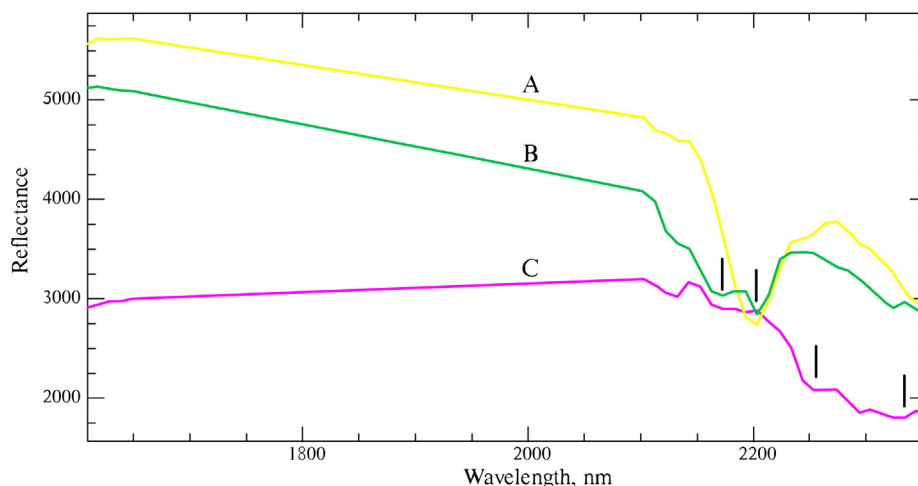

Fig. 14. Hyperion image spectra in the 1608–2355 nm wavelength region of muscovite, kaolinite and epidote. The vertical lines show the locations of important absorption features.
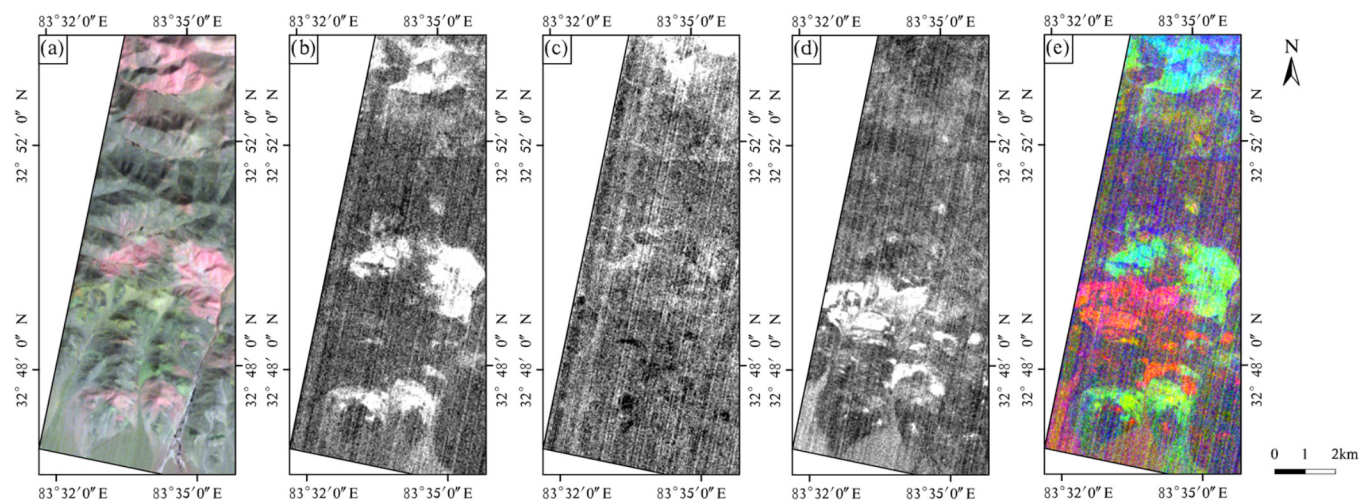
Fig. 15. (a) The Hyperion color composite image of the Tiegelong area. Hyperion bands 150 (1649 nm) = red; 205 (2204 nm) = green; 218 (2335 nm) = blue. Results of MF analysis for (b) muscovite, (c) kaolinite, and (d) epidote. (e) Color composite of fractions for epidote = red, muscovite = green, and kaolinite = blue. (For interpretation of the references to color in this figure legend, the reader is referred to the web version of this article.)

Table 5
Accuracy assessment for mineral mapping acquired using the MF method.

	Reference data				Kappa Coefficient
	Muscovite	Kaolinite	Epidote	Total	
Truly-mapped pixels	162	148	227	537	
Falsely-mapped pixels	27	0	0	27	0.89
Not-mapped	0	4	11	15	
Accuracy (%)	85.71	97.37	95.38	92.75 (Overall accuracy)	

Table 6
Separability calculations for three classes of hydrothermally altered minerals.

Classes	Kaolinite	Epidote
Muscovite	0.64	1.80
Kaolinite		1.70

function. The three classes of hydrothermally altered minerals produced from the Hyperion dataset are selected as the ROIs. The separability of the ROIs in the ASTER SWIR image is calculated. The resultant values estimate the ability of the ASTER SWIR data to spectrally discriminate among the three classes (Table 6). ROI pairs with low separability values (less than 1) should be merged (Oskouei and Busch, 2012). The classes of muscovite and kaolinite should be combined because their separability score is less than 1. Thus, only two classes of hydrothermally altered minerals can be produced from the ASTER SWIR image in the Duolong area.

4.5. Field validation

The image processing results were verified by a field reconnaissance during July 2013. Samples were collected from representative hydrothermal alteration zones associated with the known copper deposits in the Duolong area (Fig. 17). Locations were recorded by the a GPS device. Spectral reflectance measurements were obtained using SVC HR 1024, which records 1024 channels throughout the 350 to 2500 nm wavelength range (Fig. 18).

5. Discussion

Phyllically and argillically altered rocks containing alunite, kaolinite and muscovite can be mapped using the Sentinel-2A MSI data. However, it is impossible to identify propylitically altered rocks because of the breadth of the MSI band 12 (Table 1). The Crosta technique, which is based on the PCA method, has been widely employed in hydrothermally altered mineral mapping. False anomalies caused by random noise can be mixed with real altered anomalies. What is more, they cannot be effectively eliminated using an adaptive fuzzy switching filter and mean filtering (Xu et al., 2004; Brekke and Solberg, 2005). The anomaly-overlaying selection method is put forward to omit false anomalies. The information on hydroxyl-bearing minerals and iron oxides can be extracted using the combination of the Crosta technique and the anomaly-overlaying selection method.
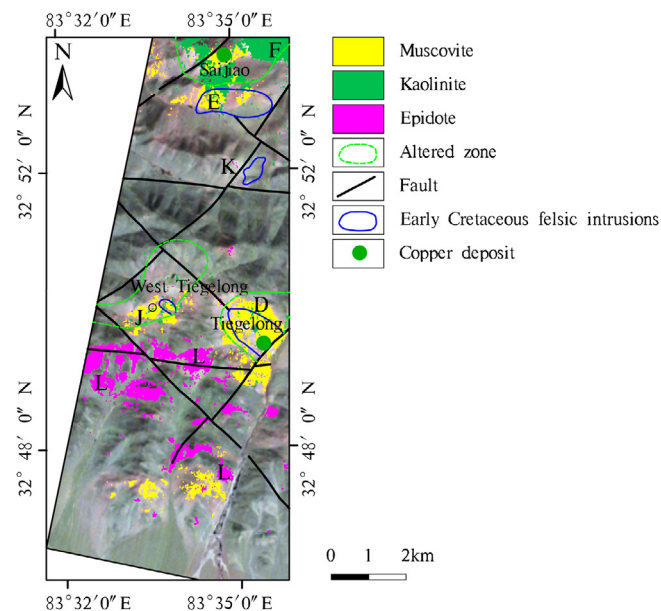

Fig. 16. Results for muscovite, kaolinite and epidote extracted from the Hyperion SWIR bands. Background image: Hyperion 150, 205, 218 (30th October 2004). Areas discussed in the text: (D) muscovite in the granitic intrusive rocks of the Tiegelong deposit; (E) muscovite inside the granodiorite in the northeastern part; (F) kaolinite around the granodiorite in the northeastern part; (J) muscovite inside and around the granite porphyry in the West Tiegelong area; (K) epidote around the granodiorite in the northeastern part; (L) epidote of the hydrothermally altered rocks in the southeastern part.
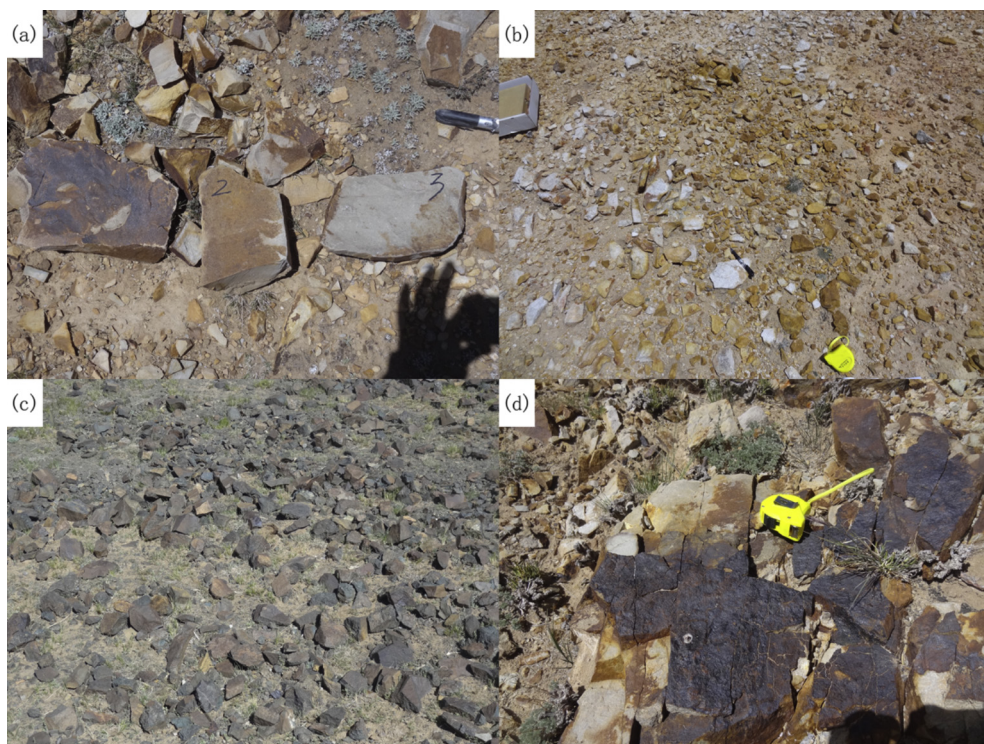
Fig. 17. Some exposures of hydrothermally altered rocks in the Duolong area. (a) muscovite in the phyllic zone of the Bolong PCD at site 1; (b) kaolinite in the argillic zone of the Saijiao PCD at site 2; (c) regional view of the propylitic zone of the Duobuza PCD at site 3; (d) limonite in the iron stained zone of the Tiegelong PCD at site 4. For the geographical locations of the sites see Fig. 7.

The spectral reflectance differences between the Al-OH and Mg-OH minerals are conspicuous in the ASTER spectra (Fig. 11). ASTER SWIR bands are applied to distinguish the Al-OH group minerals from the Mg-OH group minerals based on their spectral resolution. The ASTER image spectra are extracted by a combination of MNF, PPI and n-D Visualizer.

The MF method is used to map the two classes of hydrothermally altered minerals. The MF results are normally distributed and each anomaly is determined by a threshold value. The Al-OH group minerals in the ASTER image map correspond to the hydroxyl-bearing minerals in the MSI image map. The Mg-OH group minerals which cannot be
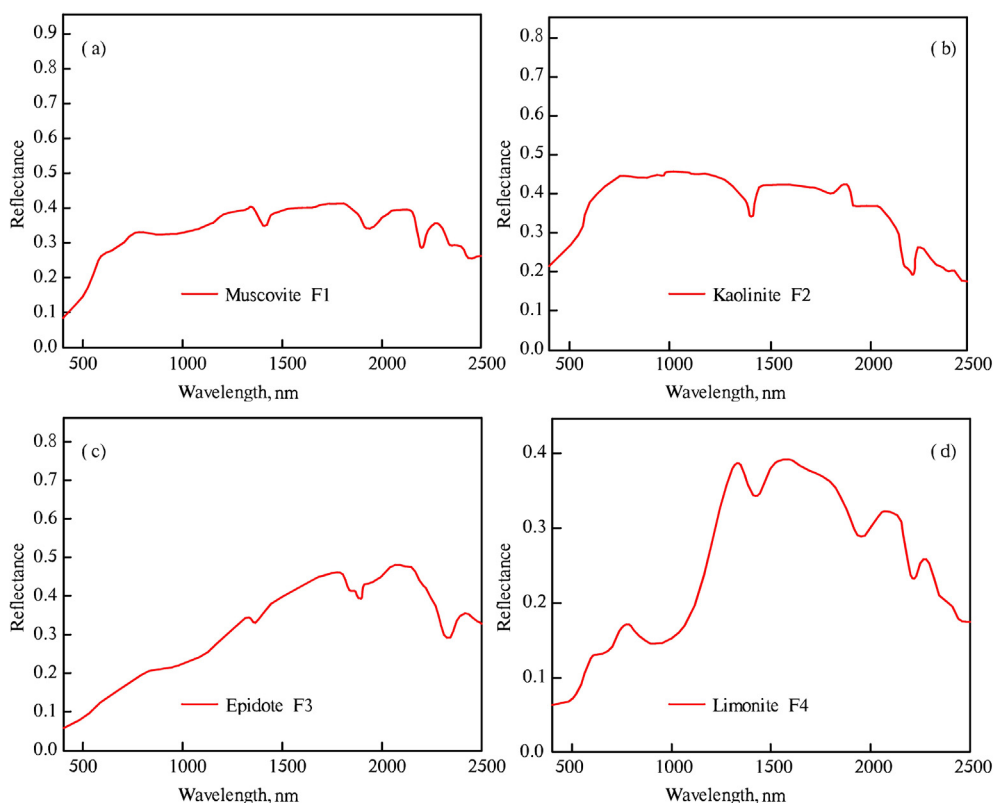

Fig. 18. The reflectance spectra of field samples from the hydrothermal alteration zones. (a) F1: field sample number 1; (b) F2: field sample number 2; (c) F3: field sample number 3; (d) F4: field sample number 4. For the geographical locations of the sites see Fig. 7.

detected using the MSI images are mapped using the ASTER SWIR bands. An ELM algorithm is also used to map the two classes of hydrothermally altered minerals.

The utilization of Hyperion data is limited by the low signal-to-noise ratio (SNR), narrow swath and site specificity. Usually, Hyperion spaceborne hyperspectral imagery is used to acquired accurate hydrothermally altered mineral mapping results. The methods of MNF, PPI and n-D Visualizer are integrated to extract the Hyperion image spectra. The spectral of the endmembers are compared with the spectra of minerals from the USGS spectral library resampled to the Hyperion channels. The advantage of this semiautomatic methodology is that no prior knowledge of the area is required. The research demonstrates that muscovite, kaolinite and epidote could be differentiated by using the Hyperion SWIR bands. An MF technique is used with the Hyperion SWIR imagery to map three classes of hydrothermally altered minerals. The accuracy the mapping results is assessed by virtual verification.

The Hyperion imagery is site-specific due to its 7.5 km coverage in the across-track direction. So it is common to combine the multispectral and hyperspectral data to map the spatial distribution of hydrothermally altered minerals. The integration of MSI, ASTER and Hyperion data can lead to the identification of key hydrothermal minerals related to the mineralization prospects. The Sentinel-2A MSI images are analyzed to map the spatial distribution of the alteration minerals (iron oxides and hydroxyl-bearing minerals). ASTER SWIR bands are used to map the Al-OH and Mg-OH minerals. The Mg-OH group minerals which cannot be detected using the MSI images are mapped using the ASTER SWIR bands. An MF technique is used with the Hyperion SWIR imagery to map muscovite, kaolinite and epidote. The integration of multispectral and hyperspectral data can enable the identification of the type of minerals and increase the reliability of remote sensing-based mineral resources exploration. Because of the not well resolved kaolinite absorption band at 2170 nm (Fig. 4) distinguishing between muscovite and kaolinite using the ASTER SWIR bands could be prone to errors. This is a new conclusion in the field.

The distribution patterns of these hydrothermal alteration zones correspond well with the hydrothermal alteration zones delineated from field reconnaissance (Li et al., 2011; Zhu et al., 2011; Zhang et al., 2014; Yang et al., 2015). PCDs are typically characterized by the potassic zone, the phyllic zone, the argillic zone and propylitic zone. Previous research has proved that the phyllic zone provides a crucial contribution to copper mineralization in the Duolong area. Accordingly, three mineralization prospects associated with felsic intrusions have been found (Fig. 7). A newest study indicates that the breccia pipes occur at the first prediction site (I, named Nadun, Fig. 7) (Zhang et al., 2016), where the kaolinite and alunite exist. Outcrops of granodiorite porphyry have been discovered by geological investigations at the second prediction site (II, Fig. 7) (Zhang et al., 2016). Felsic intrusions associated with copper mineralization have been found during field investigation (III, named West Tiegelong, Fig. 7) (Zhang et al., 2016). The potentially mineralized areas will be tested by further geological exploration.

6. Conclusions

This research attests to the significance and advantages of the synthetic application of Sentinel-2A MSI, ASTER and Hyperion data to detect hydrothermal alteration zones associated with copper mineralization in the Duolong area. Three temporal Sentinel-2A MSI images are analyzed using the Crosta technique and the anomaly-overlaying selection method to map the spatial distribution of the alteration minerals. The MF method is applied to the ASTER data for detailed hydrothermal alteration mapping. The distribution of Al-OH group minerals is spatially consistent with the distribution of hydroxyl-bearing minerals. The results of the ASTER data indicate that the Al-OH group minerals are specifically useful for exploring potentially mineralized areas associated with felsic intrusions. Information on Mg-OH group

minerals can also be extracted using ASTER data. The results indicate that both ELM algorithm and MF algorithm can used for mineral mapping. The application of Hyperion data can provide complementary information to Sentinel-2A MSI and ASTER data for hydrothermally altered mineral mapping. The methods of MNF, PPI, n-D Visualizer and MF are effectively combined to acquire more accurate hydrothermal alteration mapping results using Hyperion data. However, it is hard to use the approaches to detect the copper mineralization in heavy vegetation covering areas. This is the limitation of these methods. The overall accuracy of the image processing results reach 92.75% (*Kappa* = 0.89), indicating the validity of the methods. What is more, the distribution patterns of the hydrothermal alteration zones show a good agreement with the alteration zones identified by field investigations. The spectral reflectance measurements of the field samples verify the remote sensing results. Three mineralization prospects associated with felsic intrusions have been located. The Duolong PCD is the representative deposit of the Bangong Co-Nujiang River porphyry copper metallogenic belt of the Tibetan Plateau. The approaches and data used here are suitable for the detection of mineralization in other arid areas.

References

Amer, R., Kusky, T., El Mezayen, A., 2012. Remote sensing detection of gold related alteration zones in Um Rus area, Central Eastern Desert of Egypt. Adv. Space Res. 49 (1), 121–134.

Bedini, E., 2009. Mapping lithology of the Sarfartoq carbonatite complex, southern West Greenland, using HyMap imaging spectrometer data. Remote Sens. Environ. 113 (6), 1208–1219.

Bedini, E., 2011. Mineral mapping in the Kap Simpson complex, central East Greenland, using HyMap and ASTER remote sensing data. Adv. Space Res. 47 (1), 60–73.

Berger, M., Moreno, J., Johannessen, J.A., et al., 2012. ESA's sentinel missions in support of Earth system science. Remote Sens. Environ. 120, 84–90.

Berk, A., Bernstein, L.S., Anderson, G.P., et al., 1998. MODTRAN cloud and multiple scattering upgrades with application to AVIRIS. Remote Sens. Environ. 65 (3), 367–375.

Brekke, C., Solberg, A.H.S., 2005. Oil spill detection by satellite remote sensing. Remote Sens. Environ. 95 (1), 1–13.

Chen, C., Li, W., Su, H., et al., 2014. Spectral-spatial classification of hyperspectral image based on kernel extreme learning machine. Remote Sens. 6 (6), 5795–5814.

Cracknell, M.J., Reading, A.M., 2014. Geological mapping using remote sensing data: A comparison of five machine learning algorithms, their response to variations in the spatial distribution of training data and the use of explicit spatial information. Comput. Geosci. 63, 22–33.

Drusch, M., Del Bello, U., Carlier, S., et al., 2012. Sentinel-2: ESA's optical high-resolution mission for GMES operational services. Remote Sens. Environ. 120, 25–36.

Ducart, D.F., Crósta, A.P., Filho, C.R.S., et al., 2006. Alteration mineralogy at the Cerro La Mina epithermal prospect, Patagonia, Argentina: field mapping, short-wave infrared spectroscopy, and ASTER images. Econ. Geol. 101 (5), 981–996.

Duro, D.C., Franklin, S.E., Dubé, M.G., 2012. A comparison of pixel-based and object-based image analysis with selected machine learning algorithms for the classification of agricultural landscapes using SPOT-5 HRG imagery. Remote Sens. Environ. 118, 259–272.

Gabr, S., Ghulam, A., Kusky, T., 2010. Detecting areas of high-potential gold mineralization using ASTER data. Ore Geol. Rev. 38 (1–2), 59–69.

Goward, S.N., Masek, J.G., Williams, D.L., et al., 2001. The Landsat 7 mission: terrestrial research and applications for the 21st century. Remote Sens. Environ. 78 (1–2), 3–12.

Green, A.A., Berman, M., Switzer, P., et al., 1988. A transformation for ordering multispectral data in terms of image quality with implications for noise removal. IEEE Trans. Geosci. Remote Sens. 26 (1), 65–74.

Hewson, R., Robson, D., Mauger, A., et al., 2015. Using the Geoscience Australia-CSIRO ASTER maps and airborne geophysics to explore Australian geoscience. J. Spatial Sci. 60 (2), 207–231.

Huang, G.B., Zhu, Q.Y., Siew, C.K., 2006. Extreme learning machine: theory and applications. Neurocomputing 70 (1–3), 489–501.

Huang, H., Roy, D.P., Boschetti, L., et al., 2016. Separability analysis of Sentinel-2A multispectral instrument (MSI) data for burned area discrimination. Remote Sens. 8 (10), 873.

Hubbard, B.E., Crowley, J.K., Zimbelman, D.R., 2003. Comparative alteration mineral mapping using visible to shortwave infrared (0.4–2.5 μm) Hyperion, ALI, and ASTER imagery. IEEE Trans. Geosci. Remote Sens. 41 (6), 1401–1410.

Hunt, G.R., 1977. Spectral signatures of particulate minerals in the visible and near infrared. Geophysics 42 (3), 501–513.

Khatami, R., Mountrakis, G., Stehman, S.V., 2016. A meta-analysis of remote sensing research on supervised pixel-based land-cover image classification processes: general guidelines for practitioners and future research. Remote Sens. Environ. 177, 89–100.

Kratt, C., Calvin, W.M., Coolbaugh, M.F., 2010. Mineral mapping in the Pyramid Lake basin: hydrothermal alteration, chemical precipitates and geothermal energy potential. Remote Sens. Environ. 114 (10), 2297–2304.

Kruse, F.A., Boardman, J.W., Huntington, J.F., 2003. Comparison of airborne hyperspectral data and EO-1 Hyperion for mineral mapping. IEEE Trans. Geosci. Remote Sens. 41 (6), 1388–1400.

Langford, R.L., 2015. Temporal merging of remote sensing data to enhance spectral regolith, lithological and alteration patterns for regional mineral exploration. Ore Geol. Rev. 68, 14–29.

Li, J., Qin, K., Li, G., et al., 2011. Magmatic-hydrothermal evolution of the Cretaceous Duolong gold-rich porphyry copper deposit in the Bangongco metallogenic belt, Tibet: evidence from U-Pb and 40Ar/39Ar geochronology. J. Asian Earth Sci. 41 (6), 525–536.

Li, J.X., Qin, K.Z., Li, G.M., et al., 2013. Petrogenesis of ore-bearing porphyries from the Duolong porphyry Cu–Au deposit, central Tibet: evidence from U-Pb geochronology, petrochemistry and Sr–Nd–Hf–O isotope characteristics. Lithos 160, 216–227.

Liu, L., Zhuang, D.F., Zhou, J., et al., 2011. Alteration mineral mapping using masking and Crosta technique for mineral exploration in mid-vegetated areas: a case study in Areletuobie, Xinjiang (China). Int. J. Remote Sens. 32 (7), 1931–1944.

Liu, L., Zhou, J., Jiang, D., et al., 2013. Targeting mineral resources with remote sensing and field data in the Xiemisitai area, West Junggar, Xinjiang, China. Remote Sens. 5 (7), 3156–3171.

Liu, L., Zhou, J., Jiang, D., et al., 2016. Mineral resources prospecting by synthetic application of TM/ETM+, Quickbird and Hyperion data in the Hatu area, West Junggar, Xinjiang, China. Sci. Rep. 6, 21851.

Liu, L., Zhou, J., Han, L., et al., 2017. Mineral mapping and ore prospecting using Landsat TM and Hyperion data, Wushitala, Xinjiang, northwestern China. Ore Geol. Rev. 81, 280–295.

Lowell, J.D., Guilbert, J.M., 1970. Lateral and vertical alteration-mineralization zoning in porphyry ore deposits. Econ. Geol. 65 (4), 373–408.

Loughlin, W.P., 1991. Principal component analysis for alteration mapping. Photogramm. Eng. Remote Sens. 57 (9), 1163–1169.

Mars, J.C., Rowan, L.C., 2006. Radiometer (ASTER) data and logical operator algorithms arc, Iran, using Advanced Spaceborne Thermal Emission and Reflection Regional mapping of phyllic and argillic altered rocks in the Zagros magmatic. Geosphere 2 (3), 161–186.

Mars, J.C., Rowan, L.C., 2010. Spectral assessment of new ASTER SWIR surface reflectance data products for spectroscopic mapping of rocks and minerals. Remote Sens. Environ. 114 (9), 2011–2025.

Mas, J.F., Flores, J.J., 2008. The application of artificial neural networks to the analysis of remotely sensed data. Int. J. Remote Sens. 29 (3), 617–663.

Mielke, C., Boesche, N.K., Rogass, C., et al., 2014. Spaceborne mine waste mineralogy monitoring in South Africa, applications for modern push-broom missions: hyperion/OLI and EnMAP/Sentinel-2. Remote Sens. 6 (8), 6790–6816.

Molan, Y.E., Refahi, D., Tarashti, A.H., 2014. Mineral mapping in the Maherabad area, eastern Iran, using the HyMap remote sensing data. Int. J. Appl. Earth Obs. Geoinf. 27, 117–127.

Moore, F., Rastmanesh, F., Asadi, H., et al., 2008. Mapping mineralogical alteration using principal-component analysis and matched filter processing in the Takab area, northwest Iran, from ASTER data. Int. J. Remote Sens. 29 (10), 2851–2867.

Oskouei, M.M., Busch, W., 2012. A selective combined classification algorithm for mapping alterations on ASTER data. Appl. Geomatics 4 (1), 47–54.

Pal, M., 2009. Extreme-learning-machine-based land cover classification. Int. J. Remote Sens. 30 (14), 3835–3841.

Pour, A.B., Hashim, M., 2011. Identification of hydrothermal alteration minerals for exploring of porphyry copper deposit using ASTER data, SE Iran. J. Asian Earth Sci. 42 (6), 1309–1323.

Pour, A.B., Hashim, M., 2012a. The application of ASTER remote sensing data to porphyry copper and epithermal gold deposits. Ore Geol. Rev. 44, 1–9.

Pour, A.B., Hashim, M., 2012b. Identifying areas of high economic-potential copper mineralization using ASTER data in the Urumieh-Dokhtar Volcanic Belt, Iran. Adv. Space Res. 49 (4), 753–769.

Pour, A.B., Hashim, M., 2013. Fusing ASTER, ALI and Hyperion data for enhanced mineral mapping. Int. J. Image Data Fusion 4 (2), 126–145.

Pour, A.B., Hashim, M., van Genderen, J., 2013. Detection of hydrothermal alteration zones in a tropical region using satellite remote sensing data: Bau goldfield, Sarawak,Malaysia. Ore Geol. Rev. 54, 181–196.

Rowan, L.C., Hook, S.J., Abrams, M.J., et al., 2003. Mapping hydrothermally altered rocks at Cuprite, Nevada, using the Advanced Spaceborne Thermal Emission and Reflection Radiometer (ASTER), a new satellite-imaging system. Econ. Geol. 98 (5), 1019–1027.

Rowan, L.C., Mars, J.C., 2003. Lithologic mapping in the Mountain Pass, California area using advanced spaceborne thermal emission and reflection radiometer (ASTER) data. Remote Sens. Environ. 84 (3), 350–366.

Rowan, L.C., Simpson, C.J., Mars, J.C., 2004. Hyperspectral analysis of the ultramafic complex and adjacent lithologies at Mordor, NT, Australia. Remote Sens. Environ. 91 (3–4), 419–431.

Rowan, L.C., Mars, J.C., Simpson, C.J., 2005. Lithologic mapping of the Mordor, NT, Australia ultramafic complex by using the Advanced Spaceborne Thermal Emission and Reflection Radiometer (ASTER). Remote Sens. Environ. 99 (1–2), 105–126.

Rowan, L.C., Schmidt, R.G., Mars, J.C., 2006. Distribution of hydrothermally altered rocks in the Reko Diq, Pakistan mineralized area based on spectral analysis of ASTER data. Remote Sens. Environ. 104 (1), 74–87.

Sabins, F.F., 1999. Remote sensing for mineral exploration. Ore Geol. Rev. 14 (3–4), 157–183.

Sillitoe, R.H., 2010. Porphyry copper systems. Econ. Geol. 105 (1), 3–41.

Singh, A., Harrison, A., 1985. Standardized principal components. Int. J. Remote Sens. 6 (6), 883–896.

Sun, J., Mao, J., Beaudoin, G., et al., 2017. Geochronology and geochemistry of porphyritic intrusions in the Duolong porphyry and epithermal Cu-Au district, central Tibet: implications for the genesis and exploration of porphyry copper deposits. Ore Geol. Rev. 80, 1004–1019.

Tangestani, M.H., Moore, F., 2000. Iron oxide and hydroxyl enhancement using the Crosta Method: a case study from the Zagros Belt, Fars Province, Iran. Int. J. Appl. Earth Obs. Geoinf. 2 (2), 140–146.

Tangestani, M.H., Jaffari, L., Vincent, R.K., et al., 2011. Spectral characterization and ASTER-based lithological mapping of an ophiolite complex: a case study from Neyriz ophiolite, SW Iran. Remote Sens. Environ. 115 (9), 2243–2254.

Van der Meer, F.D., Van der Werff, H.M.A., Van Ruitenbeek, F.J.A., 2014. Potential of ESA's Sentinel-2 for geological applications. Remote Sens. Environ. 148, 124–133.

Van Der Werff, H., Van Der Meer, F., 2016. Sentinel-2A MSI and Landsat 8 OLI provide data continuity for geological remote sensing. Remote Sens. 8 (11), 883–899.

Wan, B., Guo, Q., Fang, F., et al., 2015. Mapping US urban extents from MODIS data using one-class classification method. Remote Sens. 7 (8), 10143–10163.

Xu, H., Zhu, G., Peng, H., et al., 2004. Adaptive fuzzy switching filter for images corrupted by impulse noise. Pattern Recogn. Lett. 25 (15), 1657–1663.

Xu, W., Li, C., Wang, M., et al., 2017. Subduction of a spreading ridge within the Bangong Co–Nujiang Tethys Ocean: evidence from Early Cretaceous mafic dykes in the Duolong porphyry Cu–Au deposit, western Tibet. Gondwana Res. 41, 128–141.

Yamaguchi, Y., Fujisada, H., Kudoh, M., et al., 1999. ASTER instrument characterization and operation scenario. Adv. Space Res. 23 (8), 1415–1424.

Yang, Y., Zhang, Z., Tang, J.X., et al., 2015. Mineralization, alteration and vein systems of the Bolong porphyry copper deposit in the Duolong ore concentration area, Tibet. Geol. China 42, 759–776.

Zhang, T., Yi, G., Li, H., et al., 2016. Integrating Data of ASTER and Landsat-8 OLI (AO) for Hydrothermal Alteration Mineral Mapping in Duolong Porphyry Cu-Au Deposit, Tibetan Plateau, China. Remote Sens. 8 (11), 890.

Zhang, X., Pazner, M., 2007. Comparison of lithologic mapping with ASTER, hyperion, and ETM data in the southeastern Chocolate Mountains, USA. Photogramm. Eng. Remote Sens. 73 (5), 555–561.

Zhang, Z., Chen, Y., Tang, J., et al., 2014. Alteration and vein systems of Duobuza gold-rich porphyry copper deposit, Tibet. Miner. Deposits 33 (6), 1268–1286.

Zhou, C., Yin, K., Cao, Y., et al., 2018. Landslide susceptibility modeling applying machine learning methods: a case study from Longju in the Three Gorges Reservoir area, China. Comput. Geosci. 112, 23–37.

Zhu, X.P., Chen, H.A., Ma, D.F., et al., 2011. Re-Os dating for the molybdenite from Bolong porphyry copper-gold deposit in Tibet, China and its geological significance. Acta Petrol. Sinica 27 (7), 2159–2164.